

Isolating Balanced Ocean Dynamics in SWOT Data

J. W. Skinner^{1,2}, J. Callies², A. Lawrence¹, and X. Zhang²

¹Brandeis University, Waltham, MA

²California Institute of Technology, Pasadena, CA

Corresponding author: J. W. Skinner, jskinner@caltech.edu

Key Points

- We isolate balanced sea surface height (SSH) signals in SWOT measurements using a Bayesian inversion based on Gaussian processes.
- The method fills the nadir gap and extracts meso- and submesoscale flow structures from originally noisy SSH maps.
- Tests on synthetic data generated from a high-resolution simulation illustrate the reliability of the extraction and its estimated uncertainty.

Abstract

The Surface Water and Ocean Topography (SWOT) mission provides two-dimensional sea surface height (SSH) maps at unprecedented resolution, but its signal is a combination of balanced meso- and submesoscale turbulence, unbalanced internal waves, and small-scale noise. Interpreting the meso- and submesoscale flow features captured by SWOT requires a careful isolation of the balanced signal. We present a statistical method to do so in regions where internal-wave signals are negligible, such as western boundary current regions and the Southern Ocean. Our method assumes Gaussian statistics for both the balanced flow and the noise, which we infer by fitting parametric models to the observed SSH wavenumber spectrum. Using these inferred parameters, we perform a Bayesian inversion to reconstruct swath-aligned SSH maps that fill the nadir gap. We evaluate the method using synthetic data from a high-resolution simulation with realistic SWOT-like noise added. Comparisons with the underlying model data show that our reconstruction successfully removes small-scale noise while preserving meso- and submesoscale eddies, fronts, and filaments down to a feature scale of ~ 10 km. The comparison also demonstrates that the posterior uncertainty is a reliable estimate of the error.

Plain Language Summary

The recently launched SWOT mission measures the height of the sea surface at high resolution and in two dimensions, revealing the eddies, fronts, and filaments characteristic of ocean turbulence in much finer detail than previously possible. The SWOT measurements, however, also contain small-scale errors associated with surface gravity waves, which complicates deducing the turbulent circulation. In this paper, we develop a method

to isolate the turbulent flow features in the noisy measurements. We do so by analyzing variations in the sea surface height across spatial scales and using these statistics to infer the signal, both within the swaths covered by SWOT’s measurements and across the gap around the satellite’s ground track, where only low-resolution measurements are available. We test this method using a realistic simulation of the North Atlantic, with added noise designed to mimic SWOT’s measurement characteristics. The results show that the method removes the noise contamination while preserving the characteristic features of eddies, fronts, and filaments down to a scale of around 10 km. This enables the use of SWOT data to study the role of ocean circulation at these scales in the transport of heat and carbon and in shaping ecosystems in the upper ocean.

1 Introduction

The Surface Water and Ocean Topography (SWOT) mission is providing the first high-resolution two-dimensional maps of sea surface height (SSH), enabling a global observation of the ocean across a wide range of scales (Fu et al., 2009; Morrow et al., 2019, 2018; Fu et al., 2024). Unlike previous satellite altimetry missions, which measured SSH along one-dimensional nadir tracks, SWOT’s wide-swath Ka-band Synthetic Aperture Radar Interferometer (KaRIn) instrument covers two 50-km-wide swaths, separated by a 20 km nadir gap, the center of which is sampled by a traditional Jason-class altimeter (Neeck et al., 2012; see also, Figure 1a). Together, these measurements capture the SSH variability of the ocean from the mesoscale (100 to 300 km) down to part of the submesoscale (below 100 km), providing the first two-dimensional observations of eddies, fronts, and filaments from space (Archer et al., 2025).

At the meso- and submesoscales, a large portion of the SSH variance is due to balanced flows. Mesoscale eddies are nearly geostrophically balanced and accurately described by quasi-geostrophic theory, whereas ageostrophic effects become increasingly important for submesoscale flows (e.g., Thomas et al., 2008; McWilliams, 2016; Taylor and Thompson, 2023). Theories that better capture these ageostrophic effects than quasi-geostrophic theory must be invoked, but such theories retain the idea that a balance can be used to infer the flow diagnostically from the distribution of potential vorticity (e.g., Charney, 1955; Hoskins, 1975; McWilliams and Gent, 1980; Muraki et al., 1999). We collectively refer to flows amenable to such analysis as “balanced flows” and distinguish them from unbalanced inertia–gravity waves and turbulent flow generated by unbalanced instabilities (gravitational, symmetric, inertial, etc.). The balanced part of the flow is of particular

interest because it often controls the transport of energy and tracers in the upper ocean. Mesoscale eddies dominate the kinetic energy and control lateral stirring, while submesoscale balanced motions play a key role in restratifying the water column and regulating vertical exchange of physical and biogeochemical tracers (Fox-Kemper et al., 2008; Klein and Lapeyre, 2009; Mahadevan, 2016; McWilliams, 2016; Lévy et al., 2012, 2018; Taylor and Thompson, 2023). In practice, for the ocean surface, the balanced component of the flow projects strongly onto sea surface height and can be inferred through the geostrophic and higher-order balance relations.

Isolating the balanced part of the SSH in SWOT observations is a significant challenge, however, because the measured SSH is a complex superposition of the balanced signal and a collection of other signals and noise. Zhang and Callies (2025) identified the following components in KaRIn data from typical mid-latitude open-ocean regions: balanced meso- and submesoscale signals, low-mode internal tides, small-scale noise associated with surface gravity waves, and geoid errors. The geoid errors are easily removed by subtracting a time mean, and we here focus on the Gulf Stream region, which has a strong balanced signal and comparatively weak tides. As a result, the two important remaining components are balanced signals and small-scale noise. Other western boundary current regions and the Southern Ocean should also have these characteristics and be amenable to our analysis.

The balanced signal and the noise can easily be identified in the wavenumber spectrum of SSH variance (Fig. 1b). The balanced component dominates at low wavenumbers, exhibiting a steep spectral drop-off (proportional to $k^{-4.7}$ in Fig. 1b) characteristic of balanced turbulence (e.g., Callies and Wu, 2019; and references therein). The noise component dominates at high wavenumbers and has a much flatter spectrum (proportional to $k^{-1.7}$ in Fig. 1b). The transition between the two occurs at an intermediate scale that depends on the relative amplitude of the two components (~ 38 km wavelength in Fig. 1b). In the extraction described below, we assume that the power-law form of the balanced spectrum continues beneath the noise, effectively extrapolating the steep balanced slope into the smaller, unresolved scales. This is supported by in situ observations and high-resolution simulations showing that SSH and kinetic-energy spectra typically maintain power laws down to scales of a few kilometers (e.g., Callies and Ferrari, 2013; Callies et al., 2015; Rocha et al., 2016; Callies and Wu, 2019).

While one could devise a simple spatial filter that removes the small-scale noise, we pursue a more principled approach here that separates the observed signal into its balanced and noise components based on their distinct statistics. We model both components

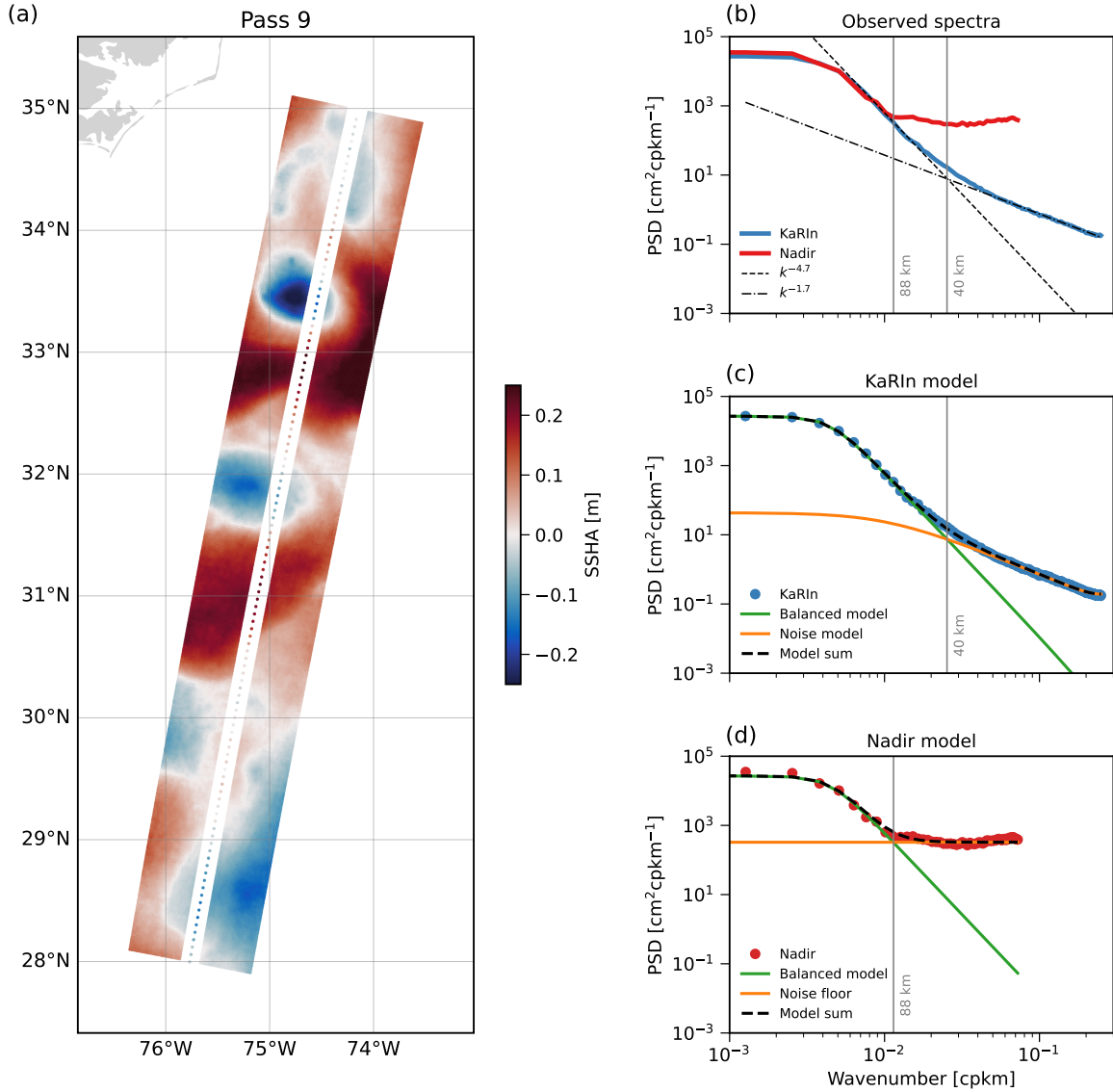


Figure 1: SWOT sea surface height anomalies (SSHA) and their statistics in the Northwest Atlantic. (a) SSHA from SWOT's KaRIn and nadir altimeters for pass 9, cycle 483 (7 April, 2023). (b) Along-track SSHA variance spectra from the two altimeters, with reference lines of $k^{-4.7}$ and $k^{-1.7}$ indicating the balanced and noise-dominated regimes in the KaRIn data. (c, d) Model fits to these spectra consisting of a balanced part and small-scale noise. For the KaRIn data, the onboard smoothing and aliasing are taken into account. The sum of the models (black dashed lines) tracks the observed spectra (dots). Vertical lines indicate the transition between the balanced and noise models: 39.5 km for KaRIn and 87.5 km for nadir.

as Gaussian processes with corresponding covariances to perform a Bayesian inversion for the balanced signal. Our method jointly uses the KaRIn and the nadir data, fills the nadir gap, provides reliable error estimates, and can be extended to additional signals and more comprehensive statistical models. The approach is based on fitting parametric models of the balanced signal and noise to the wavenumber spectrum of SSH variance for each instrument (Fig. 1b). We evaluate the performance of this extraction of the balanced signal using synthetic SWOT observations generated from a high-resolution simulation of the subtropical North Atlantic.

2 Data Sources and Processing

Our analysis focuses on the SWOT mission’s rapid-repeat phase from 26 March to 10 July 2023, during which the satellite had a 24 h repeat orbit. We use two Level-2 data products: the Level 2 KaRIn Low Rate Sea Surface Height Data Product, Version C, which provides the swath measurements at 2 km spatial resolution, and the Level 2 Nadir Altimeter Interim Geophysical Data Record (IGDR) with Waveforms, which samples SSH along the ground track with 6.8 km resolution. We use the sea surface height anomaly (SSHA) fields from both products (`ssha_karin_2` and `ssha`), which describe the deviation from the mean sea surface, with external and internal ocean tides, solid earth tides, load tides, pole tides, and the dynamic atmospheric correction removed. Combined, these two datasets cover a 120-km-wide swath: KaRIn measures two 50-km-wide swaths on either side of ground track, separated by a 20 km gap that is sampled by the nadir altimeter (Fig. 1a; SWOT, 2024, 2023).

While the method described below is widely applicable in regions with energetic balanced flows and comparatively weak internal tides, we illustrate and evaluate it in the western subtropical North Atlantic using pass 9 of the rapid-repeat phase (Fig. 2). This region offers a particularly clean test case: the balanced mesoscale–submesoscale variability is strong, high-resolution numerical simulation output is readily available, and the SWOT observations for this pass contain minimal contamination (from e.g., rain cells or other measurement artifacts).

We perform several preprocessing steps to prepare the SWOT data for analysis. First, we exclude all KaRIn and nadir observations that have non-zero quality flags. Next, we restore the full internal-tide signal—part of which is subtracted by default in the distributed products—by adding back the HRET tidal correction provided with each dataset. Although the HRET contribution is small in our focus region (at most 0.07%), we in-

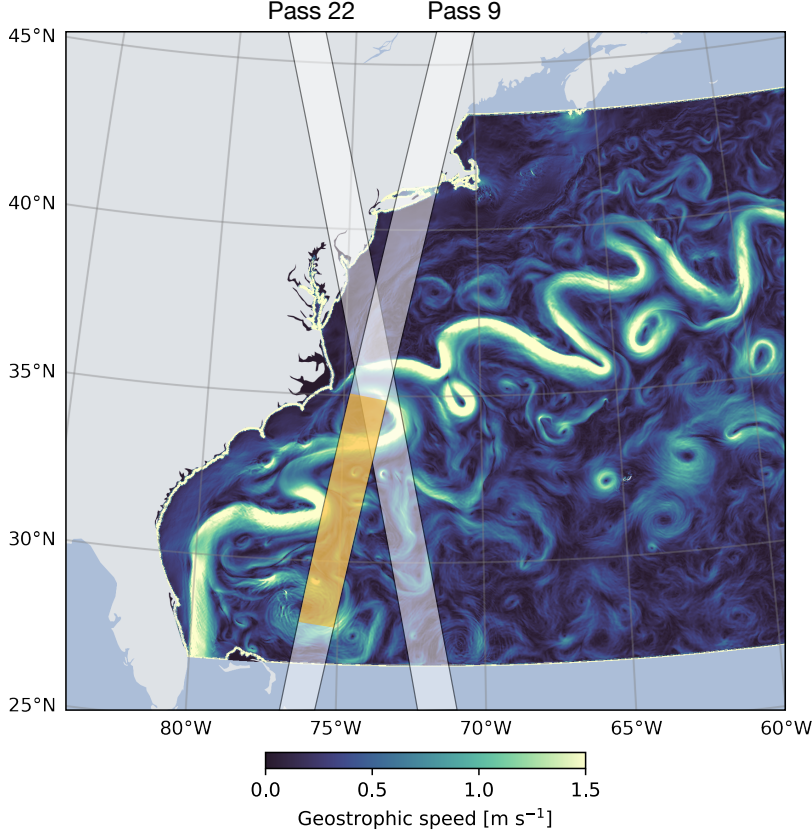


Figure 2: Location of the SWOT rapid-repeat sampling in the Northwest Atlantic, overlaid on a map of surface geostrophic speed from the numerical simulation. The section of pass 9 used in the analysis is between 29° and 35°N and is highlighted in orange.

clude it to avoid unintentionally removing any balanced low-wavenumber variance and to maintain consistency with our simulation data tests, where the full internal tide is retained.

Although the SWOT products already subtract a mean sea surface model, the mean sea surface variations due to small-scale topography were poorly constrained prior to launch (Yu et al., 2024). As a result, the time-mean SSH field contributes substantially to the signal at 10 to 50 km wavelength, producing a spectral bump (Zhang and Callies, 2025). The rapid-repeat phase provides ~ 90 revisits per pass over a three-month period, yielding a robust estimate of the time mean at small scales. At mesoscales, this time window is too short to robustly average out transient mesoscale eddies, but here the geoid is well-constrained. We therefore apply a Gaussian high-pass filter with a cutoff scale of 100 km to the time mean and subtract the resulting field from each swath. We

also remove the spatial mean, calculated from the KaRIn data and subtracted from both the KaRIn and the nadir data for each cycle, to eliminate signals associated with large-scale mixed-layer heating and cooling (Gill and Niiler, 1973).

Finally, we discard any swath in which the total SSHA variance exceeds the variance calculated from all swaths by more than an order of magnitude, and we discard swaths with significant data gaps—i.e., in which more than 20% of the data have a non-zero quality flag. These criteria effectively remove cycles contaminated by severe measurement noise or data loss. Such problematic cycles are rare in the global SWOT dataset. For our study region (between 28°N to 35°N), only two cycles of pass 9 are rejected, whereas 30 cycles of pass 22, which intersect pass 9 near the region of interest, exhibit significant data gaps.

We estimate one-dimensional along-track wavenumber spectra of SSHA variance for both instruments (Fig. 1b). The spectra are computed from SWOT tracks within the latitude range 28° to 35°N, corresponding to approximately 790 km-long segments, which provide sufficient coverage of the mesoscale band. To reduce spectral leakage, each segment is tapered with a sine-squared window, normalized to preserve the variance of a stationary signal, before a discrete Fourier transform is applied in the along-track direction. For the KaRIn data, the power spectral density (PSD) is then estimated by averaging the resulting spectrograms over each across-track pixel (both swaths) and cycle. Any across-track positions containing masked values are excluded before this averaging. For the nadir data, the spectrograms are averaged over all available cycles from the rapid-repeat phase.

Throughout this paper, spectra are shown as functions of ordinary wavenumber k (units of cpkm), the inverse of the wavelength ℓ . The angular wavenumber $2\pi k$ and its inverse are more easily associated with the scales of features; e.g., the Fourier transform of a Gaussian of width σ is a Gaussian of width σ^{-1} in angular wavenumber space and $(2\pi\sigma)^{-1}$ in ordinary wavenumber space. This conversion factor should be kept in mind when interpreting the ordinary wavenumber spectra throughout the paper. All spectra are one-sided, i.e., normalized such that

$$\langle h^2 \rangle = \int_0^\infty P(k) dk, \quad (1)$$

where h is the SSHA, angle brackets denote the average, and $P(k)$ is the PSD.

To test the balanced extraction method, we use the SSHA fields from a regional simulation of the midlatitude North Atlantic to generate synthetic SWOT data. The simulations

are performed at $(1/48)^\circ$ horizontal resolution (~ 2.3 km) (Sinha et al., 2023; Skinner et al., 2025). We sample the model’s SSHA at the same times and locations as the KaRIn and nadir measurements for SWOT pass 9 over all valid cycles, and we interpolate the simulation fields onto the observation points using cubic splines. The simulation domain spans the width of the North Atlantic, but our analysis focuses on the western North Atlantic, where SWOT passes 9 and 22 intersect the Gulf Stream (Fig. 2). In this region, the SSHA variance exceeds 0.1 m^2 (standard deviation > 30 cm), indicative of strong balanced eddies and fronts. In contrast, in less energetic regions such as the eastern North Atlantic, internal tides make a leading-order contribution to the SSHA spectra. As with the SWOT products, which have their mean sea surface removed, we subtract a long-term time mean from the simulation data. The mean is computed over the region sampled by the KaRIn swath, and we subtract the same mean value from the KaRIn and nadir samples. This ensures that the synthetic SWOT data are referenced to a consistent baseline, matching the mean-removed convention of the SWOT products.

3 Extraction of Balanced Signals

To extract the balanced signal from the SWOT data, we adopt a parametric framework similar to that of Zhang and Callies (2025). We extend their method in several ways to fully exploit the SWOT observations. First, we fit spectral models jointly to both the KaRIn and nadir measurements, enabling a consistent treatment of the complete SWOT dataset. Second, rather than prescribing the slope of the balanced spectrum, we treat it as a free parameter to be estimated directly from the data, allowing the model to adapt to more finely to the observed statistics. Third, we include a model of the onboard smoothing of KaRIn data and take the aliasing of sub-sampled signals into account. Fourth, we use the resulting covariances in a Bayesian inversion to reconstruct the balanced field across the entire swath, including the nadir gap. This framework also interpolates over masked or missing data points, using the inferred spatial covariances to provide statistically consistent estimates of the balanced field in regions without reliable observations. Together, these extensions provide a more flexible and data-driven characterization of the balanced signal and enable a comprehensive estimation of the balanced flow field.

3.1 Parametric Models for Balanced and Noise Spectra

We assume that the SSHA observations are the sum of a balanced signal and noise, and we posit that these two components are uncorrelated. The two instruments have distinct noise characteristics but sample the same balanced signal (Fig. 1b). The nadir altimeter has an approximately white noise spectrum, while KaRIn has a red noise spectrum of substantially reduced amplitude. The KaRIn onboard processing for the low-rate data furthermore smoothes the observations before sub-sampling them to 2 km, so we interpret the KaRIn signal as a smoothed sum of the balanced signal and noise. The nadir data is not smoothed onboard.

As in Zhang and Callies (2025), we adopt the following parametric models for the spectrum of the balanced signal and KaRIn's noise:

$$B(k) = \frac{A_b}{1 + (\lambda_b k)^{s_b}}, \quad N(k) = \frac{A_n}{[1 + (\lambda_n k)^2]^{\frac{s_n}{2}}}. \quad (2)$$

Here, A_b and A_n set the amplitude of the spectra, λ_b and λ_n are the wavelengths at which the spectra transition from a low-wavenumber plateau to a high-wavenumber power law, and s_b and s_n are the exponents of those power laws. Throughout, we assume that the statistics are isotropic and stationary in space and time.

We represent KaRIn's onboard smoothing as a Gaussian taper $\exp(-\frac{1}{2}\delta^2\kappa^2)$ in spectral space, where $\kappa = \sqrt{k^2 + l^2}$ is the magnitude of the wavevector (k, l) , and we set $\delta = \pi d / 2\sqrt{\ln 2}$ with $d = 2$ km the pixel size, such that the corresponding Gaussian smoother has an autocorrelation of 1/2 at a distance of $d/2 = 1$ km (Peral, 2016). Because the smoothing is two-dimensional, we need Abel transforms to calculate the impact of the smoothing on one-dimensional spectra (see Appendix A). We therefore model the KaRIn spectrum as

$$P^K(k) = \mathcal{A}[\mathcal{A}^{-1}[B(k) + N(k)](\kappa) \exp(-\delta^2\kappa^2)](k), \quad (3)$$

where \mathcal{A} denotes an Abel transform and \mathcal{A}^{-1} its inverse. The nadir data is not smoothed, so we model it simply as

$$P^N(k) = B(k) + 2\Delta\sigma^2. \quad (4)$$

The white noise derives its magnitude from the standard deviation σ of the nadir measurements and their spacing Δ .

Despite the onboard smoothing, the KaRIn data experiences some aliasing of unresolved signals by the sub-sampling to 2 km. We account for this by fitting $\sum_0^\infty P^K(|k - 2nk_N|)$ rather than $P^K(k)$ to the observed spectrum, with the rapidly converging sum truncated at $n = 2$. Aliasing is negligible for the nadir data.

We estimate the parameters A_b , λ_b , s_b , A_n , s_n , and σ from the observations by fitting the models (3) and (4) to the PSD estimated from the data. We set $\lambda_n = 100$ km because it is poorly constrained by the data and has little influence on the model fits, provided it is large enough. The remaining parameters for $B(k)$ and $N(k)$ are obtained by fitting the KaRIn spectrum, and σ is obtained by fitting the nadir spectrum while holding the parameters for $B(k)$ fixed, because the KaRIn data provide a much stronger constraint on them than the nadir measurements. All fits are performed in log-log space using a weighted least-squared method with a k^{-1} weighting factor following Lawrence and Callies (2022) and Zhang and Callies (2025). This prevents the densely sampled high-wavenumber data from dominating the fit, ensuring a stable fit across all scales.

Applying this procedure to pass 9 yields good fits to the spectra estimated from the SWOT observations (Fig. 1c,d). The fit produces a balanced spectrum that transitions from a plateau at $A_b = 2.7 \times 10^4 \text{ cm}^2 \text{ cpkm}^{-1}$ to a power law at a wavelength of $\lambda_b = 224$ km, and it estimates the spectral slope to be $s_b = 4.7$. Dividing the transition scale λ_b , which corresponds to the size of the dominant mesoscale eddies, by 2π corresponds to a spatial scale of ~ 40 km, consistent with the radius of the strongest eddies in the maps (Fig. 1a). The noise has a much lower plateau at $A_n = 43.6 \text{ cm}^2 \text{ cpkm}^{-1}$ and a smaller spectral slope of $s_n = 1.7$. The nadir noise is estimated to have an amplitude $\sigma = 5.2$ cm. The balanced and noise models intersect at 40 km for the KaRIn data and 88 km for the nadir data.

3.2 Estimating the Balanced Signal

With the parameters of the spectral models in hand, we perform a statistical estimate of the balanced component of the SSHA field. We adopt a Gaussian process framework, built on the assumption of Gaussian signal and noise statistics, to combine the observations from the KaRIn and nadir instruments. The observations, denoted \mathbf{h}_K for KaRIn and \mathbf{h}_N for the nadir altimeter, are modeled as a combination of a balanced signal at their respective locations, \mathbf{x}_K for KaRIn and \mathbf{x}_N for nadir, plus an instrument-dependent noise. For the KaRIn data, the signal is considered to be smoothed by the onboard processor, which is modeled as described above. Our goal is to estimate the balanced signal \mathbf{h}_* at a set of target locations \mathbf{x}_* . We assume that both the signal and noise components have Gaussian statistics. Under this assumption, their joint distribution with the observations forms a multivariate Gaussian. This formulation is well suited for capturing the second-order statistics (i.e., the covariance and spectrum), although higher-order moments may exhibit

non-Gaussian characteristics (see discussion below). The joint Gaussian prior distribution is given by

$$\begin{bmatrix} \mathbf{h}_K \\ \mathbf{h}_N \\ \mathbf{h}_* \end{bmatrix} \sim \mathcal{N} \left(\mathbf{0}, \begin{bmatrix} \mathbf{R}_{KK} & \mathbf{R}_{NK}^T & \mathbf{R}_{*K}^T \\ \mathbf{R}_{NK} & \mathbf{R}_{NN} & \mathbf{R}_{*N}^T \\ \mathbf{R}_{*K} & \mathbf{R}_{*N} & \mathbf{R}_{**} \end{bmatrix} \right). \quad (5)$$

The covariance matrices are obtained from the spectral models above using the Wiener–Khinchin theorem, assuming stationarity and isotropy of the statistics. With the cosine transform written as

$$\mathcal{C}[P](r) \equiv \int_0^\infty P(k) \cos(2\pi kr) dk, \quad (6)$$

the observational covariances are

$$(R_{NN})_{ij} = \mathcal{C}[B(k)](r_{ij}) + \sigma^2 \delta_{ij} \quad (7)$$

$$(R_{KK})_{ij} = \mathcal{C}[\mathcal{A}[\mathcal{A}^{-1}[B(k) + N(k)](\kappa) \exp(-\delta^2 \kappa^2)](k)](r_{ij}) \quad (8)$$

$$(R_{NK})_{ij} = \mathcal{C}[\mathcal{A}[\mathcal{A}^{-1}[B(k)](\kappa) \exp(-\frac{1}{2} \delta^2 \kappa^2)](k)](r_{ij}) \quad (9)$$

and the covariances involving the target are

$$(R_{**})_{ij} = \mathcal{C}[B(k)](r_{ij}) \quad (10)$$

$$(R_{*N})_{ij} = \mathcal{C}[B(k)](r_{ij}) \quad (11)$$

$$(R_{*K})_{ij} = \mathcal{C}[\mathcal{A}[\mathcal{A}^{-1}[B(k)](\kappa) \exp(-\frac{1}{2} \delta^2 \kappa^2)](k)](r_{ij}), \quad (12)$$

where r_{ij} denotes the distance between the points under consideration. Note that the noise only appears in the KaRIn–KaRIn and nadir–nadir covariances, and the taper appears whenever smoothed KaRIn data is involved. We evaluate these cosine and Abel transforms numerically (see Appendix A).

With this prior, the posterior distribution of the balanced SSH field \mathbf{h}_* conditioned on the observations follows from Bayes’s theorem:

$$\mathbf{h}_* | \mathbf{h}_K, \mathbf{h}_N \sim \mathcal{N}(\mathbf{m}, \mathbf{C}). \quad (13)$$

The posterior mean \mathbf{m} provides the best estimate of the balanced signal, and the posterior covariance \mathbf{C} quantifies its uncertainty. They are given by

$$\mathbf{m} = \begin{bmatrix} \mathbf{R}_{*K} & \mathbf{R}_{*N} \end{bmatrix} \begin{bmatrix} \mathbf{R}_{KK} & \mathbf{R}_{NK}^T \\ \mathbf{R}_{NK} & \mathbf{R}_{NN} \end{bmatrix}^{-1} \begin{bmatrix} \mathbf{h}_K \\ \mathbf{h}_N \end{bmatrix} \quad (14)$$

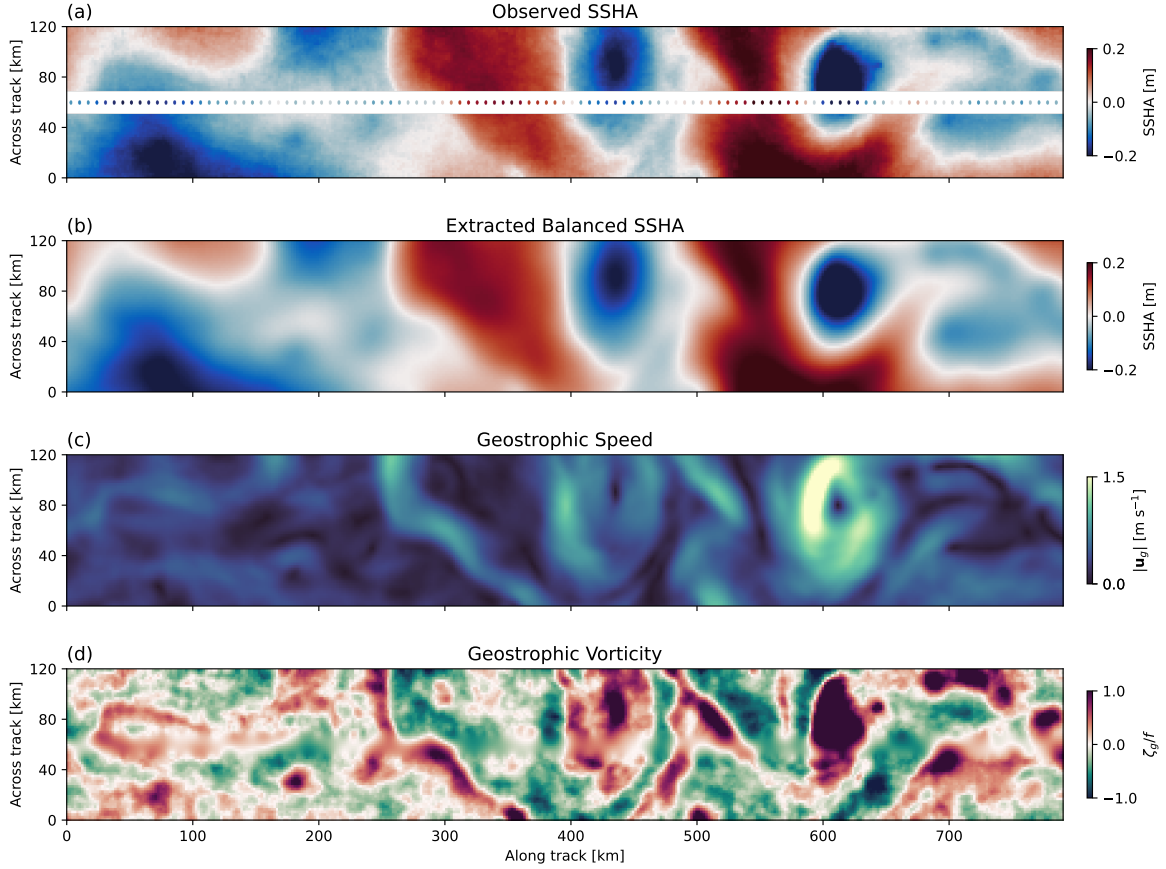


Figure 3: Balanced extraction applied to the observed SWOT SSHA field on pass 9, cycle 483 (7 April, 2023). (a) Observed SSHA data from KaRIn (swaths) and nadir (central track). (b) Extracted balanced SSHA field estimated from the observed SSHA. (c) Geostrophic speed $|\mathbf{u}_g|$ of the extracted balanced SSHA field. (d) Geostrophic vorticity ζ_g derived from the extracted balanced SSHA and normalized by the planetary vorticity f . The orientation of these maps is such that the lower left corner corresponds to the south-east corner of the patch shown in Fig. 2.

and

$$\mathbf{C} = \mathbf{R}_{**} - \begin{bmatrix} \mathbf{R}_{*K} & \mathbf{R}_{*N} \end{bmatrix} \begin{bmatrix} \mathbf{R}_{KK} & \mathbf{R}_{NK}^T \\ \mathbf{R}_{NK} & \mathbf{R}_{NN} \end{bmatrix}^{-1} \begin{bmatrix} \mathbf{R}_{*K} & \mathbf{R}_{*N} \end{bmatrix}^T. \quad (15)$$

The matrix inversion is performed using a Cholesky decomposition.

This estimation of the balanced signal, from hereon referred to as the balanced extraction, effectively separates balanced meso- and submesoscale structures from the high-wavenumber noise, as illustrated using a sample of the energetic Gulf Stream region on 7 April 2023 (Fig. 3). The SSHA data from SWOT reveal a pair of mesoscale cyclones, approximately 50 to 75 km in diameter, as well as sharp frontal features between them and in the surrounding flow space. One front, a sharp gradient in SSH, extends across the entire width of the swath and from ~ 250 to 350 km in the along-track direction. Another front can be seen between the eddies at an along-track position of ~ 500 km. These structures are superimposed by small-scale noise and are bisected by the 20 km nadir gap.

When applied to these observations, the balanced extraction yields a reconstruction that preserves the mesoscale eddies and frontal structures while suppressing small-scale noise and seamlessly bridging the nadir gap (Fig. 3b). The posterior mean field \mathbf{m} , reshaped into a map for visualization, closely resembles the original SSHA but is noticeably smoother due to the removal of the small-scale noise. The extracted balanced signal retains the sharp SSHA drops across the aforementioned fronts, although the gradients are more smoothed. Multiple small-scale eddies with a diameter of ~ 10 km can be seen, e.g., located around $(x, y) = (180 \text{ km}, 30 \text{ km})$, $(x, y) = (500 \text{ km}, 0 \text{ km})$, and $(x, y) = (250 \text{ km}, 40 \text{ km})$, where x is the along-track coordinate and y is the across-track coordinate (Fig. 3a,b). We quantify the smallest features that the balanced extraction can reconstruct below.

The dynamical structures in the balanced SSHA field are clarified by examining its derivatives, which highlight small-scale features that are less apparent in the surface height field (Fig. 3c,d). We calculate the geostrophic velocity components (in the swath-aligned coordinates) and the geostrophic speed,

$$u_g = -\frac{g}{f} \frac{\partial \eta}{\partial y}, \quad v_g = \frac{g}{f} \frac{\partial \eta}{\partial x}, \quad |\mathbf{u}_g| = \sqrt{u_g^2 + v_g^2}, \quad (16)$$

as well as the geostrophic vorticity

$$\zeta_g = \frac{\partial v_g}{\partial x} - \frac{\partial u_g}{\partial y} = \frac{g}{f} \nabla^2 \eta. \quad (17)$$

To compute the geostrophic velocities and vorticity from the balanced SSH field, we use standard second-order centered finite-difference stencils in the interior and corresponding one-sided second-order stencils at the boundaries. We have checked these calculations against fourth-order accurate stencils (5-point centered in the interior and corresponding one-sided stencils of the same order at the boundaries) and found that both approaches produce indistinguishable results in the interior, reflecting the smoothness of the extracted balanced SSH fields. The higher-order stencils introduce slightly more noise near the boundaries, so we retain the second-order formulation.

The resulting map of geostrophic speed shows regions of energetic flow around the peripheries of the eddies and along the fronts (Fig. 3c). The cyclone located at ~ 600 km along-track distance exhibits a peak geostrophic speed of 2.1 m s^{-1} , although the actual speed is expected to be lower due to deviations from geostrophic balance (because $\zeta/f \gtrsim 1$, see Fig. 3d). The corresponding geostrophic vorticity field clearly exhibits the two prominent mesoscale cyclones apparent in the SSHA field as well as a variety of much smaller-scale ~ 10 km cyclonic and anticyclonic flow features in the surrounding flow space (Fig. 3d). There are both elongated features along fronts and more circular submesoscale eddy features. The cyclonic features are noticeably stronger and more localized than the anticyclonic features.

We quantify the uncertainty in the balanced extraction by evaluating the posterior covariance \mathbf{C} from (15). The square root of the diagonal of this matrix yields the standard deviation, or the expected pointwise error, of the extraction. The spatial structure of this error reflects the sampling geometry, with the lowest uncertainty within the KaRIn swaths and the highest uncertainty at the swath edges and in the central nadir gap (Fig. 4a). In the center of the KaRIn swaths, the pointwise uncertainty is about 0.70 cm , and it rises to 0.76 cm at the location of the nadir measurements. If we withhold the nadir data, the uncertainty increases only slightly to 0.80 cm at the nadir location (Fig. 4); if we withhold the KaRIn data, it increases significantly to 2.0 cm at the nadir location.

The error can be propagated to the geostrophic velocity components and the geostrophic vorticity, which are all linear functions of the SSHA estimate. In the center of the KaRIn swaths, the uncertainty for the two velocity components is 7.5 cm s^{-1} (Fig. 4b,c) and increases to 8.5 cm s^{-1} in the nadir gap. The uncertainty of the along-track velocity u_g has a double-peaked structure around the nadir gap, which reflects that across-track SSH gradients can be estimated more accurately in the center of the nadir gap than at its edges. The uncertainty of the across-track velocity v_g has a single peak at the nadir location, and withholding the nadir data has little impact on the uncertainty of the u_g

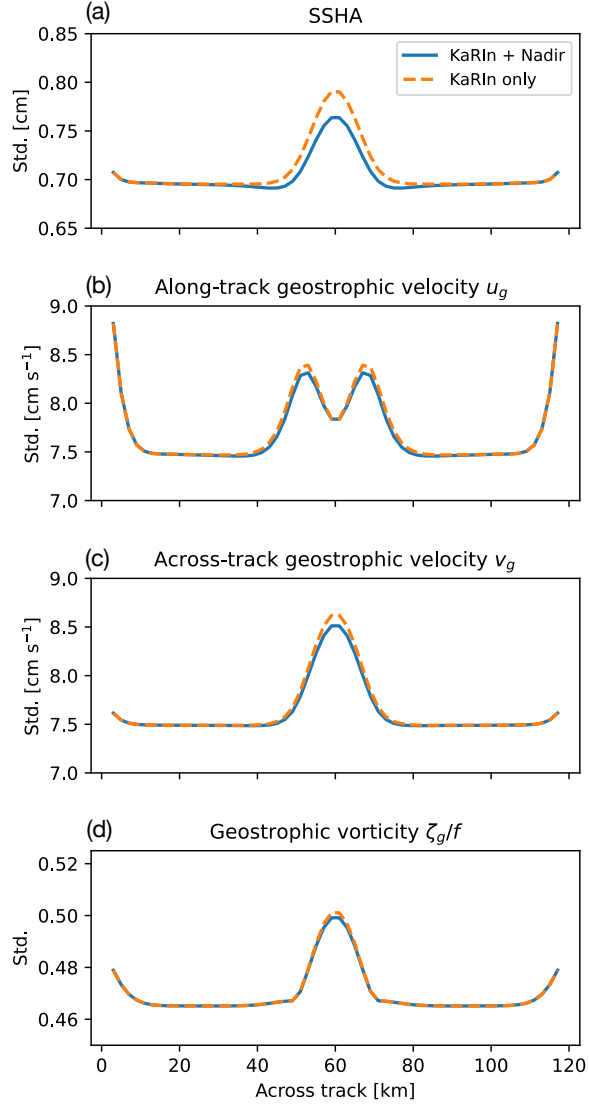


Figure 4: Cross-track profiles of the pointwise posterior uncertainty. Shown are the standard deviations for SSHA, the along-track geostrophic velocity u_g , the across-track geostrophic velocity v_g , and the normalized geostrophic vorticity ζ_g/f , derived from the posterior covariance matrix \mathbf{C} for both the full extraction and an extraction in which the nadir data is withheld. The nadir measurements are located at 60 km across-track distance.

and v_g estimates. The uncertainty in v_g from nadir data only is 15 cm s^{-1} . The uncertainty of ζ_g is $0.47f$ in the center of the KaRIn swaths and rises to $0.50f$ at the nadir location (Fig. 4d). Again, the nadir data has little impact on this uncertainty.

These posterior uncertainties indicate that many of the reconstructed flow features are statistically significant. For SSHA, the reconstruction captures mesoscale eddies with amplitudes reaching $\pm 30 \text{ cm}$, much above the uncertainty of less than 1 cm . Similarly, the balanced geostrophic velocity field resolves sharp geostrophic currents of up to 2.1 m s^{-1} against an in-swath uncertainty of 7.5 cm s^{-1} . For geostrophic vorticity, despite the uncertainty being a substantial fraction of f , many flow features rise out of this uncertainty, with values up to $3.7f$ in the strong eddy cores. We again caution that the actual currents and vorticity of the surface flow will substantially differ from their geostrophic values where $\zeta_g \gtrsim f$. The increased relative uncertainty in the geostrophic vorticity reflects the increased importance of small-scale features, which are captured by the extraction less confidently because of the dominance of noise at small scales. Nevertheless, there are many submesoscale fronts, filaments, and eddies whose geostrophic vorticity exceeds the uncertainty substantially.

The effective resolution of the balanced extraction can be assessed by comparing the power spectra of the posterior mean and the posterior uncertainty. The spectra of the original KaRIn data and the extracted SSHA fields track each other at low wavenumbers, including the steep mesoscale-to-submesoscale slope (Fig. 5). The spectrum of the extracted balanced signal diverges from the KaRIn observations and rolls off more steeply beyond $\sim 71 \text{ km}$, reflecting a strong attenuation of the extracted signal in the high-wavenumber range, where the original observation is dominated by noise. To quantify where uncertainty begins to dominate, we draw random realizations from the probability distribution of the posterior uncertainty, characterized by the covariance \mathbf{C} , by multiplying the Cholesky factor of \mathbf{C} with random vectors drawn from a standard normal distribution, and we compute the spectrum averaged over 50 realizations. We likewise estimate the spectrum of the posterior mean by drawing from its probability distribution, characterized by the covariance

$$\langle \mathbf{m} \mathbf{m}^T \rangle = \begin{bmatrix} \mathbf{R}_{*K} & \mathbf{R}_{*N} \end{bmatrix} \begin{bmatrix} \mathbf{R}_{KK} & \mathbf{R}_{NK}^T \\ \mathbf{R}_{NK} & \mathbf{R}_{NN} \end{bmatrix}^{-1} \begin{bmatrix} \mathbf{R}_{*K} & \mathbf{R}_{*N} \end{bmatrix}^T. \quad (18)$$

Because the prior covariance decomposes as $\mathbf{R}_{**} = \langle \mathbf{m} \mathbf{m}^T \rangle + \mathbf{C}$, the sum of the posterior mean and posterior uncertainty spectra reproduces the prior model for the balanced signal. At high wavenumbers, the posterior uncertainty spectrum exceeds that of the pos-

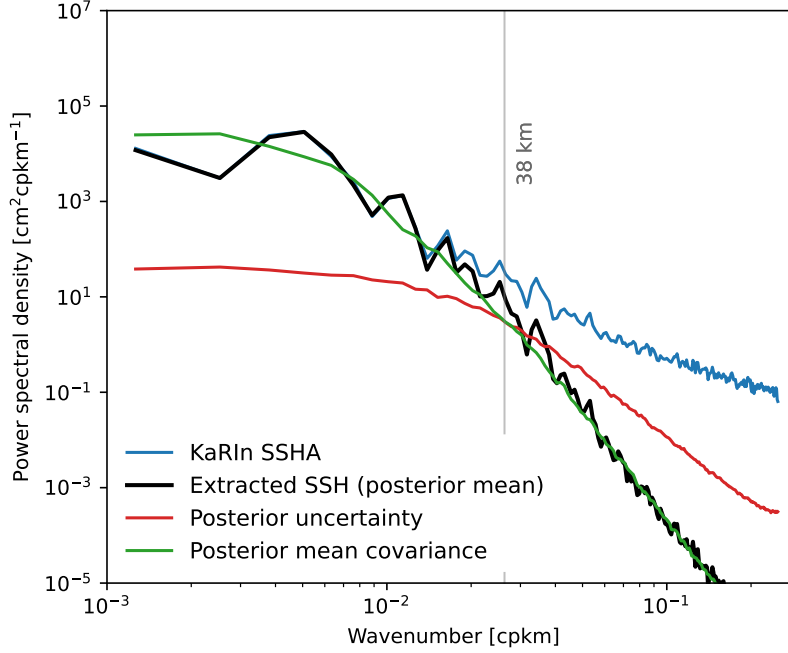


Figure 5: Along-track SSHA variance spectra for SWOT pass 9, cycle 483 (7 April, 2023). Shown are the spectra computed directly from KaRIn data (blue) and from the extracted balanced field (black). Also shown are the spectra computed from draws from the probability distributions of the posterior uncertainty (red) and the posterior mean (18) (green). The wavelength at which these two spectra intersect, the effective resolution of the extracted signal, is marked.

terior mean, indicating that the reconstruction becomes noise-dominated below wavelengths of roughly 38 km—the effective resolution limit of the extraction (Fig. 5). The steep roll-off of the mean spectrum beyond this scale reflects the inability to reconstruct the small scales in the presence of the noise. This resolution estimate is consistent with the vorticity map displaying features that are some 10 km in scale, remembering that a wavelength $\ell = 38$ km corresponds to an eddy radius of $\ell/2\pi = 6$ km (Fig. 3d).

4 Evaluation with Synthetic SWOT Data

To evaluate the balanced extraction method, we use synthetic SWOT observations generated from the numerical simulation described in Section 2, for which the corresponding “ground truth” SSHA fields are available. To generate the synthetic observations, we sample the model fields at the times of the real SWOT measurements, interpolate them to

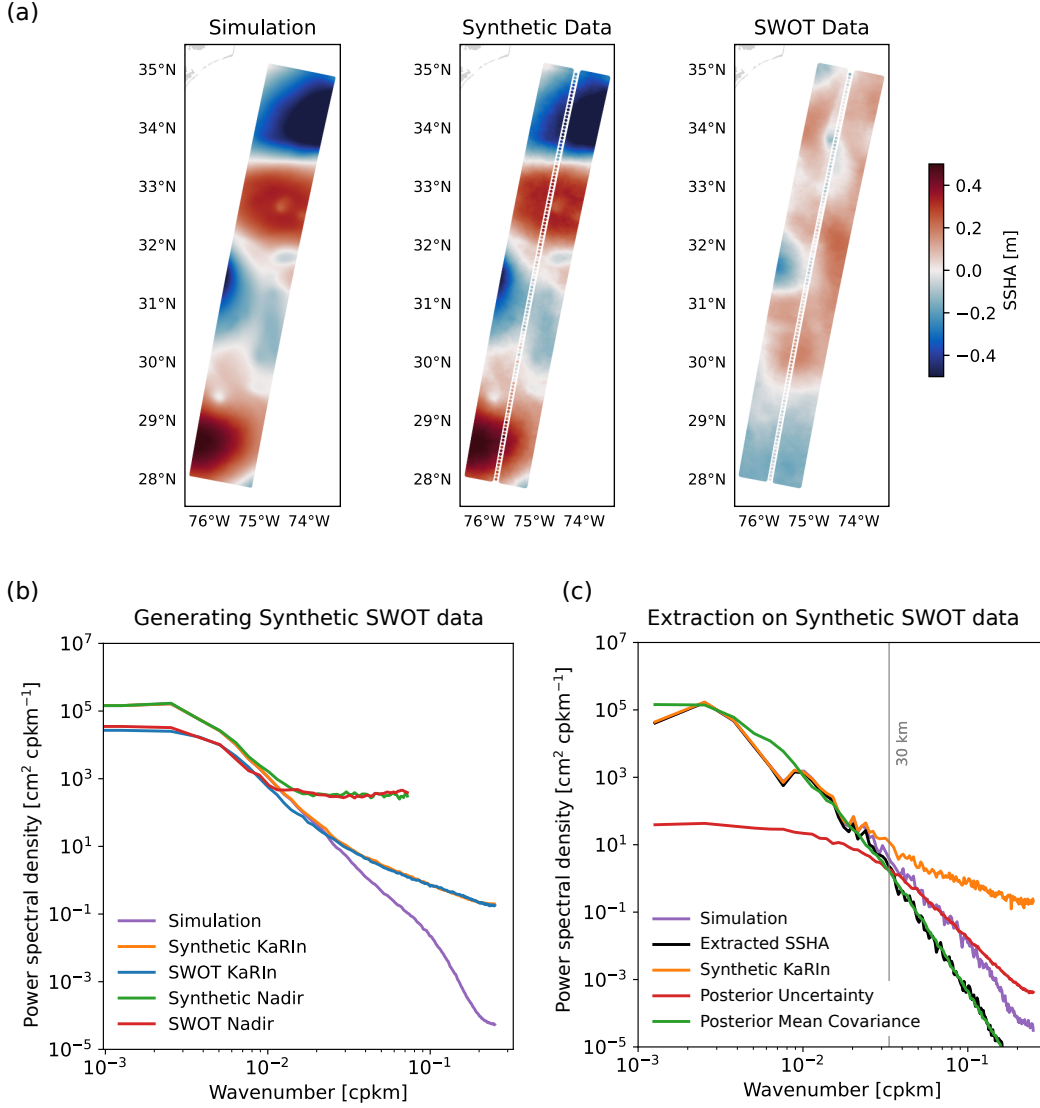


Figure 6: Synthetic SWOT observations and their statistics. (a) Maps of SSHA from the simulation (left), the corresponding synthetic SWOT observations (middle), and the real SWOT measurements (right) along pass 9 on May 10. (b) Time-averaged SSHA variance spectra from the simulation, synthetic data, and real data. (c) SSHA variance spectra from a single snapshot on May 10 from the simulation, the synthetic KaRIn observations, and the SSHA inferred from the synthetic observations by the balanced extraction. Also shown are the spectra of the posterior mean and uncertainties, obtained by averaging over samples from the mean covariance (18) and from the posterior covariance \mathbf{C} . The grey line marks the intersection between these two spectra and indicates the effective resolution of the extraction.

the exact locations of the KaRIn and nadir data points, and then add realistic noise that matches the spectral characteristics of each instrument. For the synthetic KaRIn swaths, spatially correlated noise is drawn from the posterior probability distribution characterized by the covariance matrix inferred from the fitted spectral noise model of Section 3.1. Independent realizations of the noise are generated for each SWOT cycle by multiplying vectors with elements drawn from standard normal distributions with the Cholesky factor of this covariance matrix. For the synthetic nadir tracks, we add uncorrelated white noise with the standard deviation σ inferred from the spectral fit. The resulting synthetic SWOT dataset replicates both the sampling geometry of the SWOT measurements and the high-wavenumber spectral characteristics of the SWOT observations, while the original noise-free simulation SSHA fields serve as the benchmark for evaluating the balanced extraction (Fig. 6a).

The across-track and time-averaged variance spectrum of the simulated SSHA resembles that observed by KaRIn (Fig. 6b). At low wavenumbers, the simulation has more variance than the observations, but the spectral slope in the submesoscale range, where balanced signals dominate, is comparable. The (noiseless) simulation exhibits a slight spectral hump around 10 km wavelengths, which is due to internal waves (Skinner et al., 2025). We do not attempt to model this internal-wave contribution statistically because it is overwhelmed by noise in both the real and synthetic observations; nevertheless, its presence should be noted when comparing extracted signals with the ground truth. Overall, the simulation provides a sufficiently realistic testbed for evaluating the balanced extraction.

We first assess the performance of the balanced extraction using synthetic observations of cycle 517 of pass 9 in the same region as discussed above (Fig. 2). We choose this cycle because it represents a particularly challenging test case. It features vigorous mesoscale eddies and a range of submesoscale frontal and eddy features (Fig. 7c). The synthetic SWOT data, used as the input field for the extraction, exhibits noticeable small-scale noise and the central nadir gap, compared to the ground truth, reproducing the characteristic features of SWOT observations (Fig. 7a). Despite the addition of small-scale noise and removal of the gap, the balanced extraction produces an accurate reconstruction of the original SSHA field (Fig. 7b). The comparison between the reconstructed field and the original input shows differences with a root-mean-square (RMS) of 0.7 cm (Fig. 7d and Fig. 8a). Two submesoscale cyclones at $x = 160$ and 520 km and the edge of a mesoscale cyclone around $x = 390$ km are slightly suppressed in amplitude and smoothed in their structure, but they are clearly captured by the reconstruction.

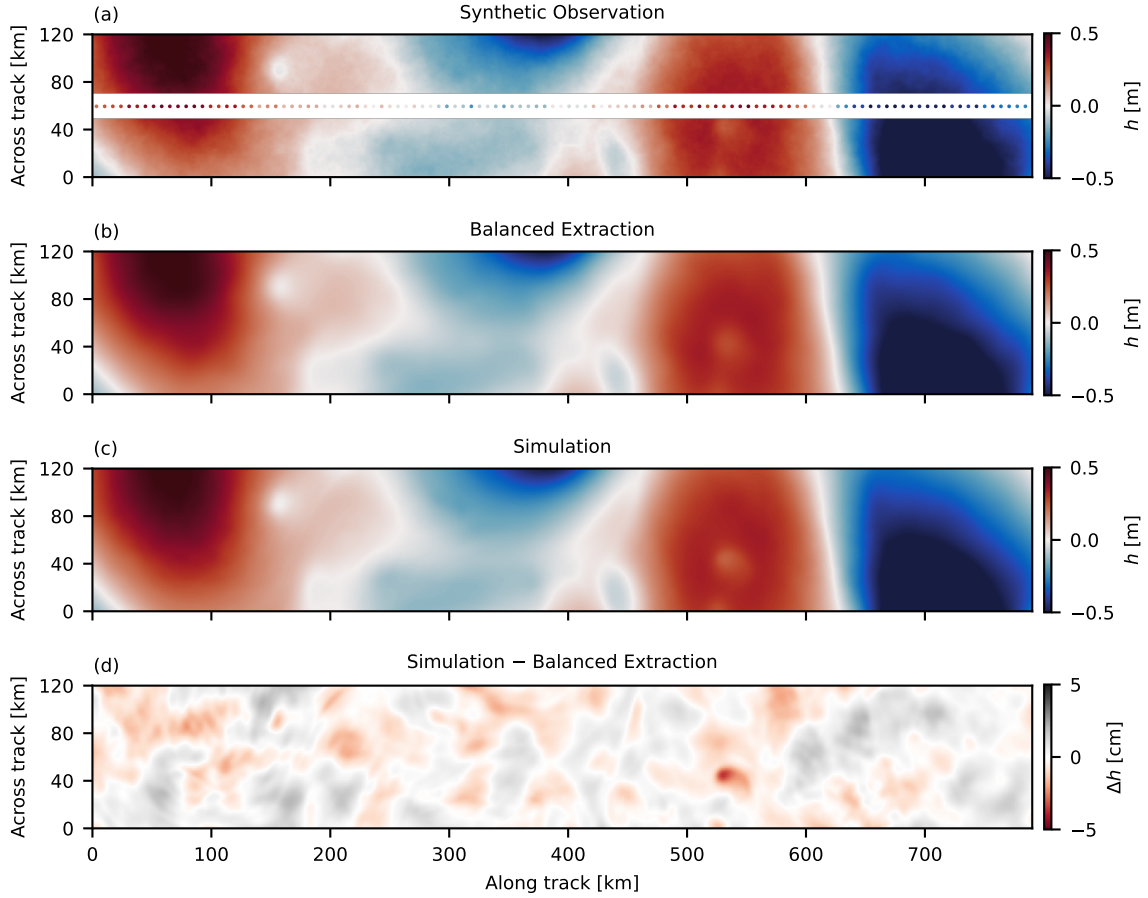


Figure 7: Reconstructing the balanced SSHA field from synthetic SWOT data. (a) Synthetic SWOT observations. (b) Extracted balanced SSHA field, estimated by applying the extraction method to the synthetic observations. (c) The ground truth from the simulation before synthetic noise was added and the SWOT sampling applied. (d) The difference between the balanced extracted fields and the simulation data. Note there is a factor of 10 difference in color scale between panels (a–c) and panel (d).

The extraction also seamlessly interpolates across the nadir gap; it reconnects the eddy structures and fronts that were fragmented by the KaRIn and nadir sampling in the observations. The balanced extraction accurately recovers the underlying ground truth signal in the gap without introducing any spurious features.

As for the real SWOT data, the uncertainty is dominated by the small scales, where noise obscures the signal (Fig. 6c). The extracted balanced signal has a spectrum that closely follows the spectrum of the ground truth at large scales but starts rolling off more steeply at around 30 km. The spectrum of the posterior uncertainty exceeds that of the posterior mean at wavelengths below an effective resolution of 30 km. This corresponds to a resolvable feature scale of some $30 \text{ km}/2\pi = 5 \text{ km}$ (a Gaussian eddy diameter of 10 km). This transition occurs at slightly smaller scales than in the real case because the balanced signal is somewhat stronger in the simulation than in the real ocean (Fig. 6b).

To evaluate the accuracy of the uncertainty estimate of the balanced extraction, we compare the RMS differences between the extracted balanced fields and (noiseless) simulation fields with the posterior standard deviation of the balanced extraction (Fig. 8). The RMS differences between the extracted balanced fields and the simulation fields are averaged both along the track and over all samples in the rapid repeat phase. The posterior standard deviation of the extraction, computed as the square root of the diagonal elements of \mathbf{C} , as above, is also averaged in the along-track direction, although there is little along-track variation. Across the swath, the posterior standard deviation of the SSHA estimate ranges from 0.71 cm in the KaRIn centers to 0.79 cm within the nadir gap (Fig. 8a). This posterior uncertainty aligns almost perfectly with the RMS differences in both magnitude and cross-swath structure.

The same comparison for the geostrophic velocity components and the geostrophic vorticity further supports that the posterior uncertainty provides a reasonable estimate for errors in the extracted signal (Fig. 8b–d). The along-track velocity u_g posterior standard deviation ranges from 8.3 cm s^{-1} in the center of the KaRIn swath to 12.5 cm s^{-1} at the edges of the swath, which is comparable to but a slight overestimate of the RMS differences that range from 7.9 to 12.6 cm s^{-1} (Fig. 8b). The along-track component v_g matches very closely, with posterior standard deviation ranging from 8.3 cm s^{-1} in the center of the KaRIn swath to 9.7 cm s^{-1} in the nadir gap, compared with RMS differences also ranging from 8.3 to 9.6 cm s^{-1} and displaying a similar structure with a noticeable increase in the nadir gap (Fig. 8c). For the geostrophic vorticity, the posterior standard deviation ranges from $0.55f$ in the center of the KaRIn swath to $0.60f$ in the nadir gap, compared with RMS differences ranging from $0.50f$ in the center of the KaRIn swath to

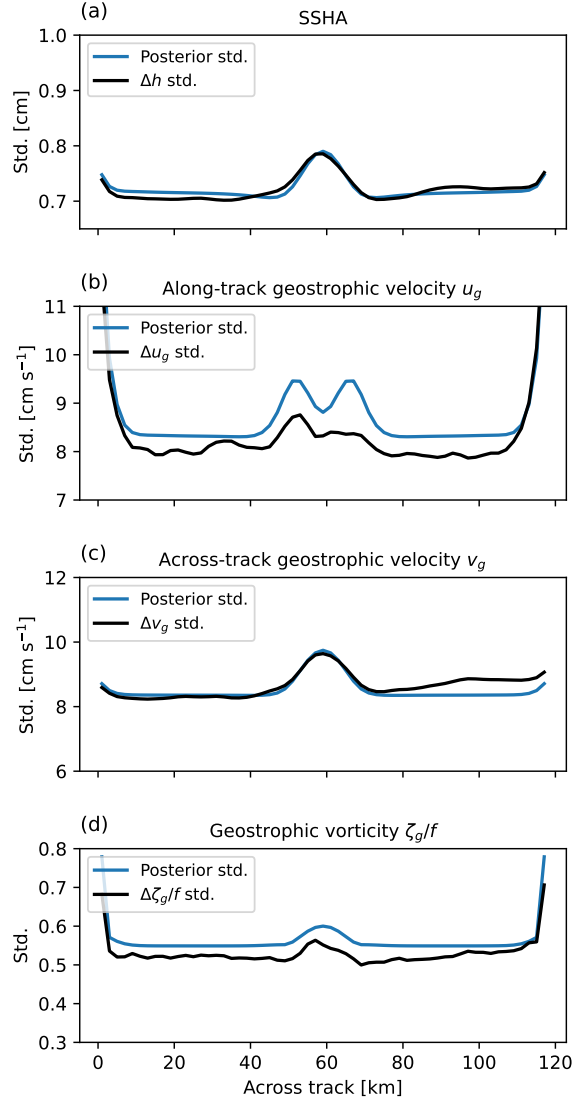


Figure 8: Comparison of posterior uncertainties and errors in the synthetic extraction. Shown are the pointwise posterior uncertainties from **C** and the errors in the balanced extraction as a function of across-track distance for SSHA, the two components of the geostrophic velocity, and normalized geostrophic vorticity. The errors are averaged over synthetic samples of the simulation corresponding to the rapid-repeat phase of SWOT.

$0.55f$ in the nadir gap (Fig. 8d). The posterior uncertainty being slightly larger than the RMS difference is expected because the balanced model extrapolates the power law to high wavenumbers ad infinitum, whereas the simulation has finite resolution and deviates substantially from this power law in its dissipation range at wavelengths <10 km (Fig. 6b,c). As a result, the simulation has less geostrophic enstrophy than predicted by the balanced model, and the RMS differences are somewhat smaller than predicted. The geostrophic vorticity statistics are discussed further below. Overall, the posterior uncertainties align well with the true reconstruction errors, demonstrating that the posterior covariance provides a good estimate of the true reconstruction uncertainty and captures the spatial variations in uncertainty across the swath.

The removal of the noise by the balanced extraction is particularly important for derived dynamical quantities such as geostrophic velocity and vorticity. The geostrophic speed computed from the raw synthetic observations displays high-amplitude striated patterns that appear to be associated with the larger-scale structures, obscuring the finer-scale fronts and eddy peripheries (Fig. 9a). This association is completely spurious, of course, given that the synthetic noise is uncorrelated to the signal. The apparent association between the noise and signal is a result of the geostrophic speed being a nonlinear diagnostic. In some regions, there are weaker signals with a similar pattern in the simulation (Fig. 9c), which appear to be due to internal waves (see the spectral hump in Fig. 6b). Extreme caution should be exercised in interpreting such patterns in the real SWOT data, and the spurious striations due to the noise should not be confused with the much weaker real signal. The balanced extraction effectively removes the dominant noise artifacts, yielding a smooth geostrophic speed field and seamlessly filling the nadir gap (Figure 9b). The extracted field is smoother than the ground truth, as expected from the spectral steepening of the expected signal at the noise-dominated scales (Fig. 6c).

The small-scale noise in the synthetic observation is further amplified in the geostrophic vorticity field, rendering the noisy data useless (Fig. 10a). In contrast, the simulation's vorticity field is dominated by energetic submesoscale cyclones with magnitudes exceeding the local planetary vorticity f , along with elongated filaments and fronts (Fig. 10c). Some contribution from internal waves is also evident at the smallest resolved scales. The balanced extraction successfully recovers a smoothed version of this ground truth simulation field (Fig. 10b): the intense cyclones, major fronts, and filaments are all retained, although slightly blurred, especially in the nadir gap. Note that the real SWOT vorticity fields obtained from the balanced extraction also follow this same overall structure (Fig. 3d). Because vorticity depends on small-scale gradients, the reconstruc-

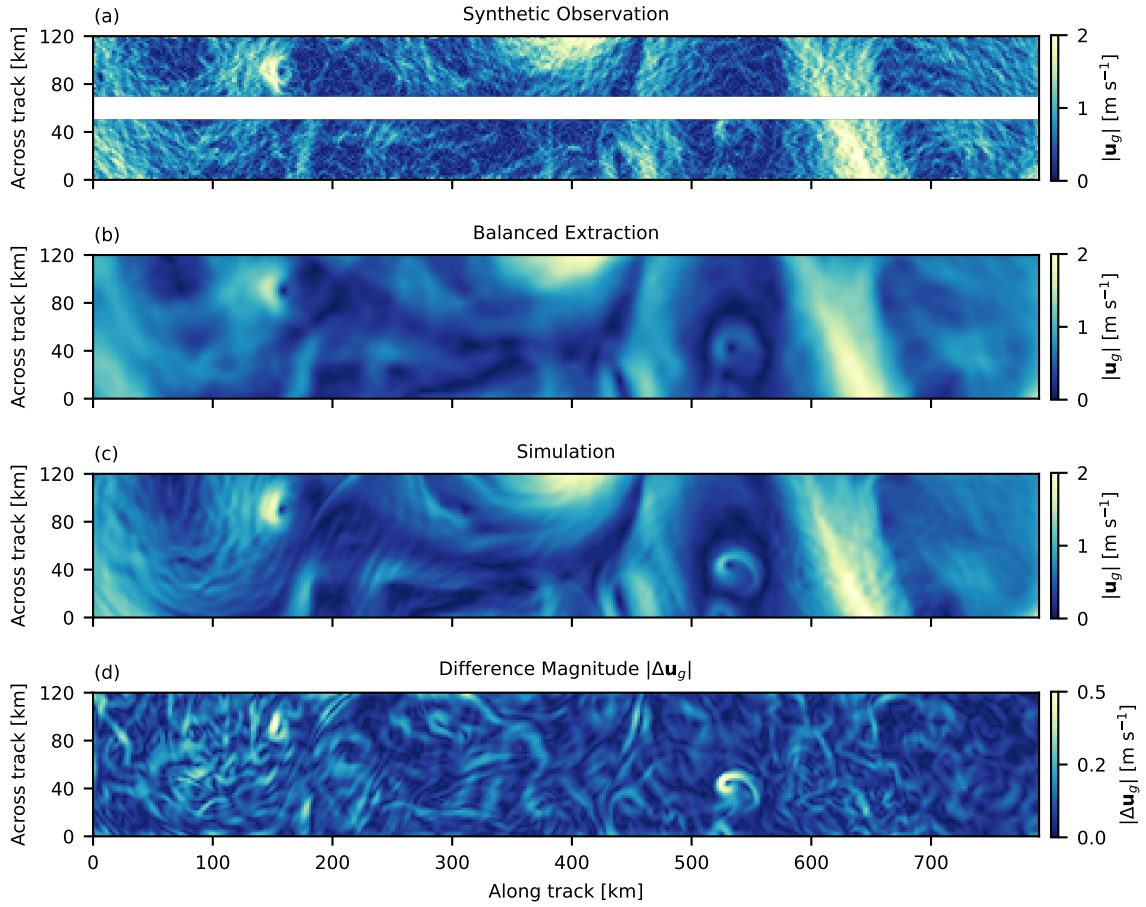


Figure 9: Evaluation of the geostrophic speed inferred from synthetic observations. (a) Geostrophic speed calculated directly from the synthetic KaRIn observations. (b) Geostrophic speed from the balanced SSHA field extracted from the synthetic observations. (c) Ground truth geostrophic speed from the simulation. (d) Magnitude of the difference in the geostrophic velocities from the balanced extraction and the ground truth. Note there is a factor 4 difference in color scale between panels (a-c) and (d).

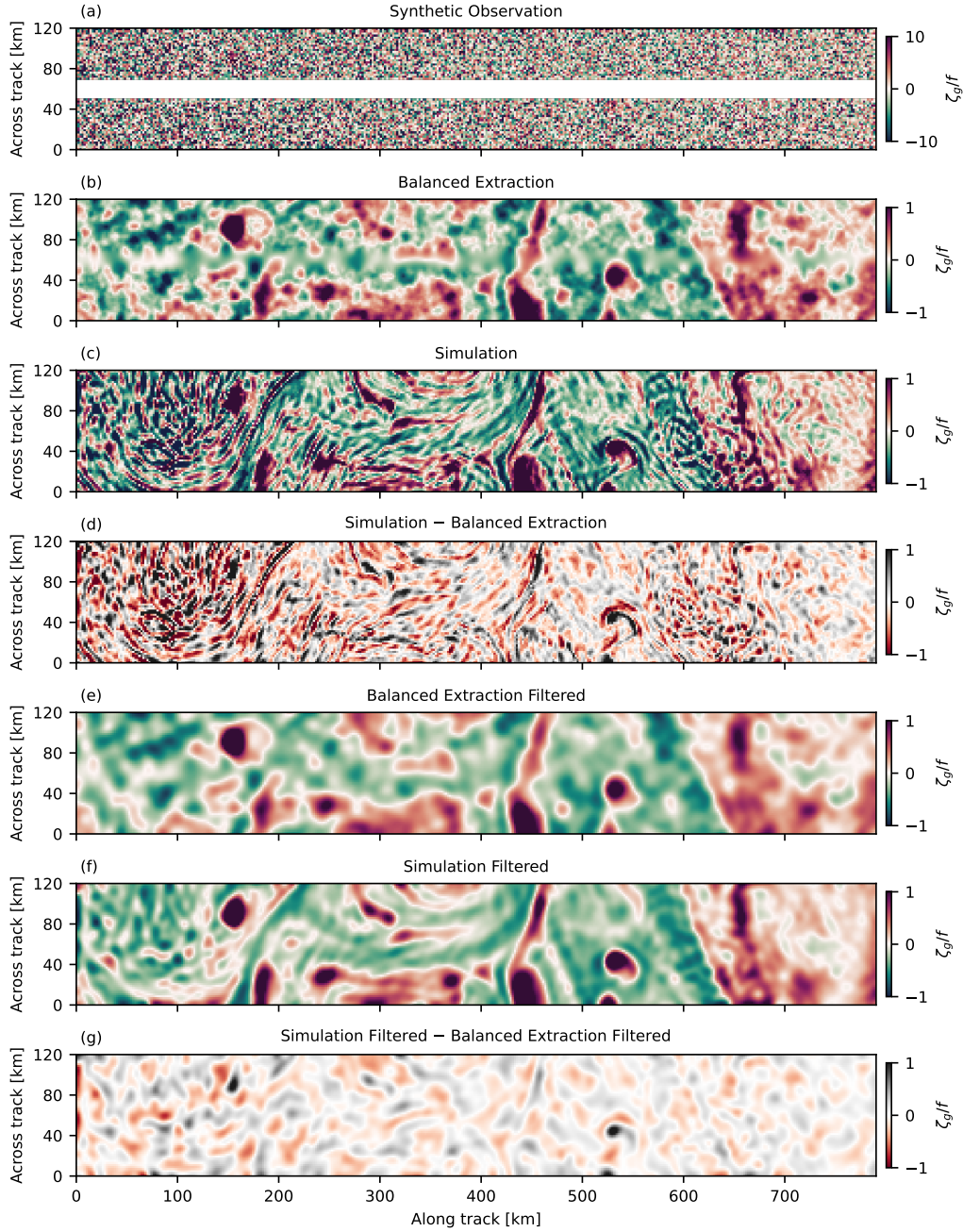


Figure 10: Evaluation of the geostrophic vorticity inferred from synthetic observations. (a) Geostrophic vorticity calculated directly from the synthetic KaRIn observations. (b) Geostrophic vorticity from the balanced SSHA field extracted from the synthetic observations. (c) Ground truth geostrophic vorticity from the simulation. (d) Difference in the geostrophic vorticity from the balanced extraction and the ground truth. (e) Geostrophic vorticity from the balanced extraction and filtered to 4 km. (f) Ground truth geostrophic vorticity from the simulation, filtered to 4 km. (g) Difference in the geostrophic vorticity from the filtered balanced extraction and the filtered ground truth.

tion carries a larger relative uncertainty, with a posterior standard deviation of approximately $0.6f$ (Fig. 8d), consistent with the RMS difference between the extracted and ground truth fields (Fig. 10d).

Because the geostrophic vorticity is dominated by the smallest resolved scales, we further compare the extraction of a filtered balanced signal to that of a filtered ground truth. We apply a Gaussian filter with a smoothing scale ρ to the target signal, such that the covariance matrices involving the target now read

$$(R_{**})_{ij} = \mathcal{C}[\mathcal{A}[\mathcal{A}^{-1}[B(k)](\kappa) \exp(-\rho^2 \kappa^2)](k)](r), \quad (19)$$

$$(R_{*N})_{ij} = \mathcal{C}[\mathcal{A}[\mathcal{A}^{-1}[B(k)](\kappa) \exp(-\frac{1}{2}\rho^2 \kappa^2)](k)](r), \quad (20)$$

$$(R_{*K})_{ij} = \mathcal{C}[\mathcal{A}[\mathcal{A}^{-1}[B(k)](\kappa) \exp(-\frac{1}{2}(\delta^2 + \rho^2) \kappa^2)](k)](r). \quad (21)$$

To ensure a like-for-like comparison, both the synthetic SWOT observations and the noiseless simulation fields are processed through the same balanced-extraction framework. We sample the simulation at the full set of target locations, including in the nadir gap, and apply neither noise nor taper in the data covariance. We set $\rho/2\pi = 4$ km, roughly corresponding to the effective resolution inferred above (Fig. 6c). As expected, the correspondence between the extracted signal and the ground truth is much improved by the smoothing (Fig. 10e,f). Many of the submesoscale eddies, fronts, and filaments at this smoothing scale are captured by the extraction at this scale. The RMS difference is reduced to $0.18f$ (Fig. 10g).

The ability to obtain reliable statistics of the surface vorticity field is highly desirable, as these statistics provide a fundamental diagnostic of balanced turbulence. They quantify the intensity of mesoscale and submesoscale eddies, reveal asymmetries between cyclonic and anticyclonic motions, and characterize the structure of eddy–eddy interactions, intermittency, and coherent vortices that mediate energy transfer across scales (e.g., McWilliams, 1984, 1985; Chelton et al., 2011; Shcherbina et al., 2013). Accurately recovering these statistics from SWOT observations is therefore highly useful for testing competing theories of turbulence, constraining the energy transfer at meso- and submesoscales, and evaluating the realism of ocean circulation models. The vorticity statistics are expected to be skewed and heavy tailed, and they must be evaluated carefully to ensure that data processing does not distort them in unrecognized ways (e.g., Baker and Gibson, 1987; Sardeshmukh and Penland, 2015; Gaultier et al., 2016; Martin and Gommenginger, 2017).

Comparing the probability distribution functions (PDFs) of geostrophic vorticity ζ_g/f between the extracted fields and the ground truth simulation data quantifies the reliabil-

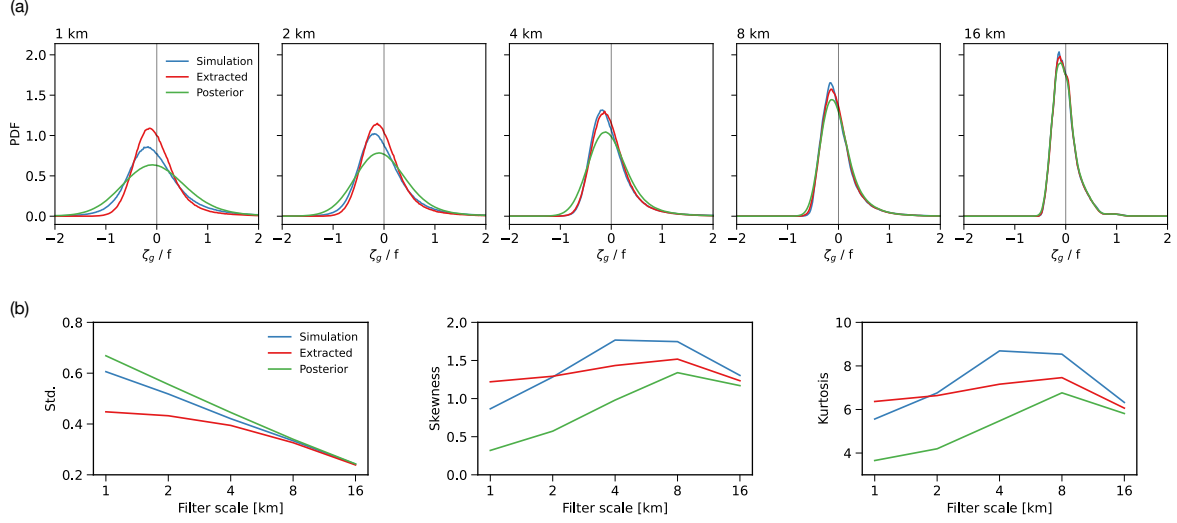


Figure 11: Statistics of the geostrophic vorticity ζ_g from the simulation and balanced extraction at different smoothing scales. (a) Probability distribution functions (PDFs) of normalized geostrophic vorticity ζ_g/f , averaged over the rapid-repeat phase. Shown are PDFs for the ground-truth simulation fields (blue), the balanced fields extracted from the synthetic SWOT observations (posterior mean, red), and samples from the posterior distribution (green). Curves are shown for progressively increasing spatial smoothing scales from 1 to 16 km. (b) The standard deviation, skewness, and kurtosis of the PDFs as a function of smoothing scale.

ity of these statistics. We apply the extraction with varying smoothing scales $\rho/2\pi = 1, 2, 4, 8$, and 16 km, and we compute PDFs from the smoothed ground truth, from the extracted fields (the posterior mean), and from 20 samples drawn from the posterior distribution, with statistics accumulated over all samples of the rapid-repeat phase. As expected, the PDF of the balanced extraction aligns closely with that of the ground truth for the most smoothed fields, and they progressively diverge as the smoothing scale is reduced (Fig. 11). As the smoothing scale drops below the effective resolution of the balanced extraction, the extracted signal has a substantially reduced variance because it does not capture the small scales that are dominated by noise in the synthetic observations. This additional variance is captured by the posterior uncertainty; in fact, the posterior PDF has slightly too much variance because the balanced model has somewhat more variance at the smallest resolved scales, as discussed above (Fig. 6b,c).

Despite the assumption of Gaussian statistics in the extraction method, the extracted signal captures some of the non-Gaussian character of the underlying geostrophic vor-

ticity field where the data constraints are strong (Fig. 11). The simulation has a positive skewness of 1.8 when filtered to 4 km, and the extracted signal (the posterior mean) has a skewness of 1.4. The full posterior PDF is less skewed, with a value of 1.0, because the part of the signal that is not constrained by the data is filled in with a Gaussian process, biasing the posterior PDF toward a normal distribution. The same effect is exhibited by the kurtosis: the simulation has wide tails, which is captured to a degree by the balanced extraction. At 4 km, the kurtosis is 8.6 for the simulation, 7.2 for the extracted signal (posterior mean), and 5.5 for the posterior PDF. As the smoothing scale is reduced, the simulation becomes more Gaussian, presumably due to the emergence of an internal-wave signal at the smallest resolved scales (Fig. 10c). The extracted signal does not capture this behavior because these scales are severely under-resolved, and the statistics are dominated by the more non-Gaussian larger scales. As a result, both skewness and kurtosis are overestimated (Fig. 11). The posterior PDF, which fills in the missing information with a Gaussian signal, instead provides a lower bound on the skewness and kurtosis.

5 Discussion

To study balanced meso- and submesoscale turbulence using SWOT data, their SSH signature must be isolated from other components of the signal. The method presented here separates the observed signal into two components, one due to balanced flows and one due to small-scale noise. A Bayesian inversion is developed that models these two components as Gaussian processes with distinct statistics inferred from wavenumber spectra. This inversion provides reliable best estimates as well as uncertainties for the balanced part of the signal, as demonstrated by analyzing synthetic observations of simulation output. In the Northwest Atlantic region considered here, the inversion produces an estimate of the balanced signal with an effective resolution of 38 km, corresponding to a feature scale of 6 km, enabling it to capture submesoscale eddies, fronts, and filaments. This resolution scale depends on the relative amplitude of the balanced signal and noise and will therefore vary across the world ocean.

The present extraction method assumes that the signal has no substantial contribution from internal waves, which limits its applicability to western boundary current regions and the Southern Ocean. Zhang and Callies (2025) estimated that low-mode internal tides contribute substantially to the SWOT signal in some 70 % of the regions sampled during the rapid-repeat phase. The present method can be extended to allow for such

signals by adding more terms to the covariance function. These additional terms would aim to characterize the spatial structure of the additional signals, and it would allow the inversion to distinguish them from the rest of the signal to the degree that this spatial structure is distinct. Given the narrowband nature of low-mode internal tides (e.g., Ray and Zaron, 2016), this approach should be able to separate them from the broadband balanced signal. Taking advantage of the tides’ narrowband nature in the frequency domain and applying the extraction simultaneously to multiple cycles could further improve estimates. Other approaches such as harmonic fits (e.g., Zaron, 2019), neural nets trained on simulations (e.g., Wang et al., 2022; Xiao et al., 2023; Gao et al., 2024), or model-based predictions (Yadidya et al., 2025) could also be used to remove the internal-tide before further analysis of the balanced signal.

Another limitation of the present approach is that it models the balanced signal as a Gaussian process, ignoring the known non-Gaussian statistics of balanced meso- and submesoscale turbulence. While the present method does recover some of these non-Gaussian statistics where the data constraint is strong, employing a non-Gaussian prior might help better preserve sharp fronts and filaments in the estimate. Approaches that learn such non-Gaussian statistics from simulation output may produce sharper submesoscale features (e.g., Tréboutte et al., 2023; Febvre et al., 2024; Martin et al., 2025). But the degree to which the simulation output is consistent with the SWOT data is not currently understood, and the potential for model error biasing the estimates should be kept in mind in applications.

Despite this room for improvement, the present method is transparent and produces robust estimates of the balanced signal. As such, it enables the study of the dynamics of meso- and submesoscale turbulence where it is energetic and internal tides are sufficiently weak. It also offers a robust framework in which the realism of simulation output can be evaluated to understand to what degree these simulations capture the physics of meso- and submesoscale turbulence.

Open Research

For the SWOT data we use the Level-2 KaRIn Basic Low Rate SSH v2.0 doi.org/10.5067/SWOT-SSH-2.0 and SWOT Level-2 Nadir IGDR v2.0 doi.org/10.5067/SWOT-NALT-IGDR-1.0 which are available from NASA PO.DAAC (SWOT, 2024, 2023). For the simulations outputs, we use the model described by Sinha et al. (2023) and Skinner et al. (2025). The analysis code for spectral fitting and Gaussian-process reconstruction, along with figure

scripts, is hosted on GitHub github.com/jwskinner/SWOT-balanced-extraction.

Acknowledgments

This work was supported by NASA grant 80NSSC23K0345, a Simons Foundation Pivot Fellowship, and by grant NSF PHY-2309135 to the Kavli Institute for Theoretical Physics (KITP). This work used high-performance computing at the San Diego Super Computing Centre (San Diego Supercomputer Center, 2022) through allocation PHY-230189 from The Advanced Cyberinfrastructure Coordination Ecosystem: Services & Support (ACCESS) program, which is supported by National Science Foundation grants #2138259, #2138286, #2138307, #2137603, and #2138296. The authors thank Patrice Klein, Andrew Thompson, Dimitris Menemenlis, Hector Torres, and Jinbo Wang for helpful discussions.

A Two-dimensional smoothing

From the observations, we estimate one-dimensional spectra, which are directly related by a cosine transform to the covariances used in the extraction. But we need to represent the two-dimensional smoothing by the onboard processor and the two-dimensional smoothing of the target signal. We therefore need to transform between the observed one-dimensional spectra and the two-dimensional spectral space in which the smoothing is applied as a Gaussian taper.

Assuming isotropy, a one-dimensional spectrum $P(k)$ can be converted to the two-dimensional spectrum $P_2(k, l)$ and the radial spectrum $P_r(\kappa)$. We normalize the spectra such that

$$\int_0^\infty P(k) dk = \int_{-\infty}^\infty \int_{-\infty}^\infty P_2(k, l) dk dl = \int_0^\infty P_r(\kappa) d\kappa. \quad (22)$$

Because $dk dl = \kappa d\kappa d\theta$, the two-dimensional and radial spectra are related by

$$2\pi\kappa P_2(k, l) = P_r(\kappa). \quad (23)$$

The one-dimensional spectrum is (twice) the integral of the two-dimensional spectrum over one dimension, such that the one-dimensional spectrum can be related to the radial spectrum as follows:

$$P(k) = 2 \int_{-\infty}^\infty P_2(k, l) dl = \frac{2}{\pi} \int_0^\infty \frac{P_r(\kappa)}{\kappa} d\kappa = \frac{2}{\pi} \int_k^\infty \frac{P_r(\kappa)}{\sqrt{\kappa^2 - k^2}} d\kappa \equiv \mathcal{A}[P_r(\kappa)](k). \quad (24)$$

This is an Abel transform, and the inverse Abel transform gives

$$P_r(\kappa) = -\kappa \int_{\kappa}^{\infty} \frac{P'(k)}{\sqrt{k^2 - \kappa^2}} dk \equiv \mathcal{A}^{-1}[P(k)](\kappa), \quad (25)$$

where the prime denotes a derivative. This allows us to go back and forth between one-dimensional spectra and radial spectra.

To represent the onboard smoothing, we apply an inverse Abel transform to $B(k) + N(k)$ to calculate the two-dimensional spectrum of the balanced signal plus noise, which we then multiply by the Gaussian taper $\exp(-\frac{1}{2}\delta^2\kappa^2)$ before applying the Abel transform to go back to a one-dimensional spectrum, resulting in (3). This recipe can be used for the covariance between any fields, with any smoothing applied to them.

While some Abel transforms can be done analytically, e.g., that of the Matérn noise model $N(k)$, we need to rely on numerical transforms in general. We implement the forward transform \mathcal{A} by discretely sampling the spectrum at a uniform wavenumber grid from 0 to $n/2L$ with spacing L^{-1} , approximating $P_r(\kappa)$ as linear between sampling points and then evaluating the integral analytically for each sampling interval. For the inverse transform \mathcal{A}^{-1} , we first calculate $P'(k)$ using second-order accurate finite differences on the same wavenumber grid before following the same approach as for the forward transform. The cosine transform \mathcal{C} to obtain the covariance function is performed using the type-I discrete cosine transform (DCT-I; e.g., Strang, 1999) on the same wavenumber grid. In all calculations, we use $L = 5000$ km and $n = 100\,000$.

References

- Archer, M., J. Wang, P. Klein, G. Dibarboure, L.-L. Fu (2025) Wide-swath satellite altimetry unveils global submesoscale ocean dynamics. *Nature* 640 (8059), 691–696.
- Baker, M. A., C. H. Gibson (1987) Sampling turbulence in the stratified ocean: Statistical consequences of strong intermittency. *Journal of Physical Oceanography* 17 (10), 1817–1836.
- Callies, J., R. Ferrari (2013) Interpreting energy and tracer spectra of upper-ocean turbulence in the submesoscale range (1–200 km). *Journal of Physical Oceanography* 43 (11), 2456–2474.
- Callies, J., R. Ferrari, J. M. Klymak, J. Gula (2015) Seasonality in submesoscale turbulence. *Nature communications* 6 (1), 6862.
- Callies, J., W. Wu (2019) Some expectations for submesoscale sea surface height variance spectra. *Journal of Physical Oceanography* 49 (9), 2271–2289.

- Charney, J. (1955) [The Use of the Primitive Equations of Motion in Numerical Prediction](#). *Tellus* 7 (1), 22–26.
- Chelton, D. B., M. G. Schlax, R. M. Samelson (2011) Global observations of nonlinear mesoscale eddies. *Progress in oceanography* 91 (2), 167–216.
- Febvre, Q., J. Le Sommer, C. Ubelmann, R. Fablet (2024) [Training Neural Mapping Schemes for Satellite Altimetry with Simulation Data](#). *Journal of Advances in Modeling Earth Systems* 16 (7), e2023MS003959.
- Fox-Kemper, B., R. Ferrari, R. Hallberg (2008) [Parameterization of Mixed Layer Eddies. Part I: Theory and Diagnosis](#). *Journal of Physical Oceanography* 38 (6), 1145–1165.
- Fu, L.-L., D. Alsdorf, E. Rodriguez, R. Morrow, N. Mognard, J. Lambin, P. Vaze, T. Lafon (2009) The SWOT (Surface Water and Ocean Topography) mission: Spaceborne radar interferometry for oceanographic and hydrological applications. *Proceedings of OCEANOBS* 9, 21–25.
- Fu, L.-L. et al. (2024) The surface water and ocean topography mission: A breakthrough in radar remote sensing of the ocean and land surface water. *Geophysical Research Letters* 51 (4), e2023GL107652.
- Gao, Z., B. Chapron, C. Ma, R. Fablet, Q. Febvre, W. Zhao, G. Chen (2024) [A Deep Learning Approach to Extract Balanced Motions from Sea Surface Height Snapshot](#). *Geophysical Research Letters* 51 (7), e2023GL106623.
- Gaultier, L., C. Ubelmann, L.-L. Fu (2016) The challenge of using future SWOT data for oceanic field reconstruction. *Journal of Atmospheric and Oceanic Technology* 33 (1), 119–126.
- Gill, A. E., P. P. Niiler (1973) [The Theory of the Seasonal Variability in the Ocean](#). *Deep Sea Research and Oceanographic Abstracts* 20 (2), 141–177.
- Hoskins, B. J. (1975) [The Geostrophic Momentum Approximation and the Semi-Geostrophic Equations](#). *Journal of the Atmospheric Sciences* 32 (2), 233–242.
- Klein, P., G. Lapeyre (2009) [The Oceanic Vertical Pump Induced by Mesoscale and Submesoscale Turbulence](#). *Annual Review of Marine Science* 1 (Volume 1, 2009), 351–375.
- Lawrence, A., J. Callies (2022) Seasonality and spatial dependence of mesoscale and submesoscale ocean currents from along-track satellite altimetry. *Journal of Physical Oceanography* 52 (9), 2069–2089.
- Lévy, M., R. Ferrari, P. J. Franks, A. P. Martin, P. Rivière (2012) Bringing physics to life at the submesoscale. *Geophysical Research Letters* 39 (14).

- Lévy, M., P. J. Franks, K. S. Smith (2018) The role of submesoscale currents in structuring marine ecosystems. *Nature communications* 9 (1), 4758.
- Mahadevan, A. (2016) The Impact of Submesoscale Physics on Primary Productivity of Plankton. en. *Annual Review of Marine Science* 8 (1), 161–184.
- Martin, A. C., C. Gommenginger (2017) Towards wide-swath high-resolution mapping of total ocean surface current vectors from space: Airborne proof-of-concept and validation. *Remote Sensing of Environment* 197, 58–71.
- Martin, S. A., G. E. Manucharyan, P. Klein (2025) [Generative Data Assimilation for Surface Ocean State Estimation from Multi-Modal Satellite Observations](#). *Journal of Advances in Modeling Earth Systems* 17 (8), e2025MS005063.
- McWilliams, J. C. (1984) The emergence of isolated coherent vortices in turbulent flow. *Journal of Fluid Mechanics* 146, 21–43.
- McWilliams, J. C. (1985) Submesoscale, coherent vortices in the ocean. *Reviews of Geophysics* 23 (2), 165–182.
- McWilliams, J. C. (2016) Submesoscale currents in the ocean. *Proceedings of the Royal Society A: Mathematical, Physical and Engineering Sciences* 472 (2189), 20160117.
- McWilliams, J. C., P. R. Gent (1980) [Intermediate Models of Planetary Circulations in the Atmosphere and Ocean](#). *Journal of the Atmospheric Sciences* 37 (8), 1657–1678.
- Morrow, R., D. Blumstein, G. Dibarboure (2018) Fine-scale altimetry and the future SWOT mission. *New frontiers in operational oceanography*, 191–226.
- Morrow, R. et al. (2019) Global observations of fine-scale ocean surface topography with the surface water and ocean topography (SWOT) mission. *Frontiers in Marine Science* 6, 232.
- Muraki, D. J., C. Snyder, R. Rotunno (1999) [The Next-Order Corrections to Quasi-geostrophic Theory](#). *Journal of the Atmospheric Sciences* 56 (11), 1547–1560.
- Neeck, S. P., E. J. Lindstrom, P. V. Vaze, L.-L. Fu (2012) Surface water and ocean topography (SWOT) mission. In: *Sensors, systems, and next-generation satellites XVI*. Vol. 8533. SPIE, 111–120.
- Peral, E (2016) KaRIn: Ka-band radar interferometer onboard processor (OBP) algorithm theoretical basis document (ATBD). *Jet Propulsion Laboratory Document D-79130, Initial Release* 72.
- Ray, R. D., E. D. Zaron (2016) [M₂ Internal Tides and Their Observed Wavenumber Spectra from Satellite Altimetry](#). *Journal of Physical Oceanography* 46 (1), 3–22.

- Rocha, C. B., T. K. Chereskin, S. T. Gille, D. Menemenlis (2016) Mesoscale to submesoscale wavenumber spectra in Drake Passage. *Journal of Physical Oceanography* 46 (2), 601–620.
- San Diego Supercomputer Center (2022) *Triton Shared Computing Cluster*. Service.
- Sardeshmukh, P. D., C. Penland (2015) Understanding the distinctively skewed and heavy tailed character of atmospheric and oceanic probability distributions. *Chaos: An Interdisciplinary Journal of Nonlinear Science* 25 (3).
- Shcherbina, A. Y., E. A. D’Asaro, C. M. Lee, J. M. Klymak, M. J. Molemaker, J. C. McWilliams (2013) Statistics of vertical vorticity, divergence, and strain in a developed submesoscale turbulence field. *Geophysical Research Letters* 40 (17), 4706–4711.
- Sinha, A., J. Callies, D. Menemenlis (2023) [Do Submesoscales Affect the Large-Scale Structure of the Upper Ocean?](#) *Journal of Physical Oceanography* 53, 1025–1040.
- Skinner, J., A. Lawrence, J. Callies (2025) Characterizing Ocean Flows with the Scattering Transform. *arXiv preprint arXiv:2505.00819*.
- Strang, G. (1999) The discrete cosine transform. *SIAM review* 41 (1), 135–147.
- SWOT (2023) *SWOT Level 2 Nadir Altimeter Interim Geophysical Data Record with Waveforms Version 1.0*.
- SWOT (2024) *SWOT Level 2 KaRIn Low Rate Sea Surface Height Data Product*.
- Taylor, J. R., A. F. Thompson (2023) Submesoscale dynamics in the upper ocean. *Annual Review of Fluid Mechanics* 55 (1), 103–127.
- Thomas, L. N., A. Tandon, A. Mahadevan (2008) Submesoscale processes and dynamics.
- Tréboutte, A., E. Carli, M. Ballarotta, B. Carpentier, Y. Faugère, G. Dibarboure (2023) [KaRIn Noise Reduction Using a Convolutional Neural Network for the SWOT Ocean Products](#). *Remote Sensing* 15 (8), 2183.
- Wang, H., N. Grisouard, H. Salehipour, A. Nuz, M. Poon, A. L. Ponte (2022) [A Deep Learning Approach to Extract Internal Tides Scattered by Geostrophic Turbulence](#). *Geophysical Research Letters* 49 (11), e2022GL099400.
- Xiao, Q., D. Balwada, C. S. Jones, M. Herrero-González, K. S. Smith, R. Abernathey (2023) [Reconstruction of Surface Kinematics from Sea Surface Height Using Neural Networks](#). *Journal of Advances in Modeling Earth Systems* 15 (10), e2023MS003709.
- Yadidya, B., B. K. Arbic, J. F. Shriver, E. D. Zaron, M. C. Buijsman, L. Carrère, M. Tchilibou, T. Uchida (2025) *Advancing Internal Tide Correction for SWOT Cal/Val: The Role of Ocean Forecasts*.
- Yu, Y., D. T. Sandwell, G. Dibarboure (2024) [Abyssal Marine Tectonics from the SWOT Mission](#). *Science* 386 (6727), 1251–1256.

- Zaron, E. D. (2019) [Baroclinic Tidal Sea Level from Exact-Repeat Mission Altimetry](#). *Journal of Physical Oceanography* 49 (1), 193–210.
- Zhang, X., J. Callies (2025) Assessing submesoscale sea surface height signals from the SWOT mission. *arXiv preprint arXiv:2505.09856*.